Analytic and finite difference modelling of DAS fiber data from moment tensor sources

Matt Eaid and Kris Innanen

ABSTRACT

Distributed acoustic sensing has become a prevalent technology for reservoir monitoring, and has potential for applications in earthquake seismology. In preparation for advanced applications of these datasets such as imaging and inversion, we develop two methods for forward modeling DAS datasets generated by moment tensor type sources. The first is an efficient analytic modeling algorithm well-suited to modeling large datasets of DAS-microseismic direct arrivals. Another paper in this issue uses this algorithm for generation of a datasets used as input for a machine learning study for source mechanism estimation. The second method we develop is a full 3D finite-difference method based on the velocity-stress method.

INTRODUCTION

Distributed acoustic sensing (DAS) is a rapidly advancing technology for seismic acquisition, especially in reservoir monitoring settings. Its use of noninvasive optical fibers to make measurements of the strain induced by propagating seismic wavefields offers many advantages in these settings. Chief among theses is their ability to be placed in active treatment wells during reservoir treatments such as hydraulic fracturing (Webster et al., 2013). DAS is also attractive for earthquake seismology studies (Lindsey et al., 2017; Yu et al., 2019), due in large part to the opportunity to leverage subsea telecommunication fiber optics, mitigating problems associated with the continental deployment bias of traditional seismology recording equipment.

The seismic signals generated by earthquakes and fractures can be modeled by considering moment tensor source mechanisms which are a function of the fracture mechanics (Aki and Richards, 2002). As the application of DAS for reservoir monitoring and seismology studies increase, methods for modeling the signals generated by moment tensor sources and recorded by DAS fibers become increasingly important. In this paper we develop two methods for modeling DAS signals generated by moment tensor source mechanisms. The first is an extension of analytic approach of Aki and Richards (2002) to strain wavefields. The second is the extension of the velocity-stress finite-difference method to computing the strain field required for DAS modeling. To validate our methods, we then compare our modeled wavefields to a field data DAS-microseismic record.

SIMULATION OF DAS DATA

Distributed acoustic sensing employs optical fibers to sense the strain,

$$\epsilon_{ij} = \frac{1}{2}\left(\frac{\partial u_i}{\partial x_j} + \frac{\partial u_j}{\partial x_i}\right) \tag{1}$$

induced by propagating seismic waves. However, due to the rigidity of the optical fibers used in DAS systems these fibers are only sensitive to components of the seismic wavefield inducing normal strains in the tangential direction of the fiber, ϵ_{tt}. Therefore, DAS is inherently a single component, and directional, recording technology. The tangential response of the DAS fiber is computed through projection of the strain tensor onto the fiber,

$$\epsilon_{tnb} = \mathbf{R}(s)\epsilon_{xyz}\mathbf{R}(s)^{\mathrm{T}} \tag{2}$$

where ϵ_{xyz} is the strain tensor in the field coordinate system, ϵ_{tnb} is the strain tensor in the coordinates of the fiber, and $\mathbf{R}(s)$ is an operator transformng between the two systems defiend as,

$$\mathbf{R}(s) = \begin{bmatrix} \hat{\mathbf{t}}(s)\cdot\hat{\mathbf{x}} & \hat{\mathbf{t}}(s)\cdot\hat{\mathbf{y}} & \hat{\mathbf{t}}(s)\cdot\hat{\mathbf{z}} \\ \hat{\mathbf{n}}(s)\cdot\hat{\mathbf{x}} & \hat{\mathbf{n}}(s)\cdot\hat{\mathbf{y}} & \hat{\mathbf{n}}(s)\cdot\hat{\mathbf{z}} \\ \hat{\mathbf{b}}(s)\cdot\hat{\mathbf{x}} & \hat{\mathbf{b}}(s)\cdot\hat{\mathbf{y}} & \hat{\mathbf{b}}(s)\cdot\hat{\mathbf{z}} \end{bmatrix}. \tag{3}$$

The normal tangential component of the strain tensor ϵ_{tnb} is,

$$\begin{aligned} \epsilon_{tt}(s) = (\hat{\mathbf{t}}\cdot\hat{\mathbf{x}})^2\epsilon_{xx} + 2(\hat{\mathbf{t}}\cdot\hat{\mathbf{x}})(\hat{\mathbf{t}}\cdot\hat{\mathbf{y}})\epsilon_{xy} + 2(\hat{\mathbf{t}}\cdot\hat{\mathbf{x}})(\hat{\mathbf{t}}\cdot\hat{\mathbf{z}})\epsilon_{xz} \\ +(\hat{\mathbf{t}}\cdot\hat{\mathbf{y}})^2\epsilon_{yy} + 2(\hat{\mathbf{t}}\cdot\hat{\mathbf{y}})(\hat{\mathbf{t}}\cdot\hat{\mathbf{z}})\epsilon_{yz} + (\hat{\mathbf{t}}\cdot\hat{\mathbf{z}})^2\epsilon_{zz} \end{aligned} \tag{4}$$

where s is the arclength along the fiber, $\hat{\mathbf{t}}$ is the tangent direction of the fiber at s and $\hat{\mathbf{x}}$, $\hat{\mathbf{y}}$, and $\hat{\mathbf{z}}$ are the field coordinates. Equation (4) clearly expresses the strain response of the fiber as a function of the fiber geometry. Commonly, straight fibers are deployed in vertical wells for VSP acquisition resulting in fibers only sensitive in the z-direction and $\epsilon_{tt} = \epsilon_{zz}$. However, fibers can be shaped on both a large scale (for example tracking a horizontal well), and a small scale (wound in some characteristic shape such as a helix). This exposes the fiber to a different portion of the wavefield, and perhaps enhances its sensitivity, if these other wavefield components contain significant energy.

The DAS fiber does not supply local point measurements of the strain. In practice, due to the weak response of the fiber on a local scale, the strain response is averaged over a length of fiber to improve the signal-to-noise ratio of the recorded. This length of fiber, L, is known as the gauge length. The gauge length averaged response of the fiber to a propagating wavefield at a fixed time t is,

$$d(s) = \int_{-L/2}^{L/2} W(s-s', L)\epsilon_{tt}(s')ds' \tag{5}$$

where $W(s-s', L)$ is an averaging operator, which in this paper is defined as,

$$W(s,L) = \begin{cases} 1/L, & -L/2 < s < L/2 \\ 0, & \text{otherwise} \end{cases} . \tag{6}$$

Thus to simulate DAS datasets requires a geometric model for the fiber, computation of the strain field in the field coordinate system $(\hat{\mathbf{x}}, \hat{\mathbf{y}}, \hat{\mathbf{z}})$, and then projection of that strain onto the fiber. In this paper we are interested in modeling the response of DAS fibers to moment tensor type sources so that we may model the datasets recorded in seismology studies or during hydraulic fracture treatments. We consider both analytic and numerical simulations in this study.

ANALYTIC EXPRESSIONS FOR STRAIN FROM A MOMENT TENSOR SOURCE

Perhaps the most important features in microseismic data, containing information about the source location and source mechanism, are the direct arrivals. Analytic methods provide a means for the efficient modelling of these direct arrivals and can provide important insights into how source mechanics influence the recorded data. Aki and Richards (2002) develop equations for modelling the displacement generated by the excitation of a moment tensor source M_{pq},

$$\begin{aligned} u_i = \frac{1}{4\pi\rho}\frac{15m\gamma_i - 3t\gamma_i - 6\gamma_i'}{r^4}\int_{r/\alpha}^{r/\beta}\tau s(t-\tau)d\tau \\ + \frac{1}{4\pi\rho\alpha^2}\frac{6m\gamma_i - t\gamma_i - 2\gamma_i'}{r^2}s(t-r/\alpha) - \frac{1}{4\pi\rho\beta^2}\frac{6m\gamma_i - t\gamma_i - 3\gamma_i'}{r^2}s(t-r/\beta) \\ + \frac{1}{4\pi\rho\alpha^3}\frac{m\gamma_i}{r}\dot{s}(t-r/\alpha) - \frac{1}{4\pi\rho\beta^3}\frac{m\gamma_i - \gamma_i'}{r}\dot{s}(t-r/\beta) \end{aligned} \tag{7}$$

where we have made use of the simplifying identities,

$$m = \gamma_p M_{pq}\gamma_q \qquad \delta_{pq}M_{pq} = \sum_p M_{pp} = \mathrm{tr}(\mathbf{M}) = t \qquad \delta_{in}\gamma_q M_{qn} = \gamma_q M_{qi} = \gamma_i'$$

and where, $\gamma_i = x_i/r$, $s(t-r/v)$, and $\dot{s}(t-r/v)$ are the directional cosine, a source time function with velocity v, and its time derivative $\dot{s}$ respectively.

Modelling DAS microseismic data requires analytic expressions of the strain propagated by moment tensor type sources. The strain tensor in equation (1) suggests that this requires derivatives of the form $\partial u_i/\partial x_j$. Therefore, spatial derivatives of the expressions for the analytic displacement developed by Aki and Richards (2002), provide the key expressions required for development of the analytic strain tensor. The identities,

$$\frac{\partial r^{-n}}{\partial x_j} = -n\frac{\gamma_j}{r^{(n+1)}} \qquad \frac{\partial \gamma_i}{\partial x_j} = \frac{\delta_{ij} - \gamma_i\gamma_j}{r}$$

$$\frac{\partial m\gamma_i}{\partial x_j} = \frac{2\gamma_i\gamma_j' - 3m\gamma_i\gamma_j + m\delta_{ij}}{r} \qquad \frac{\partial \gamma_i'}{\partial x_j} = \frac{M_{ij} - \gamma_i'\gamma_j}{r}$$

$$\frac{\partial s(t - r/v)}{\partial x_j} = -\dot{s}(t - r/v)\frac{\gamma_j}{v} \qquad \Gamma_{ij} = \frac{1}{2}(\gamma_i\gamma_j' + \gamma_i'\gamma_j)$$

ease the computation of the spatial derivatives. Using these identities to compute the derivatives of equation (7) provides one of the two terms in the strain tensor of equation (1). The other term can be computed by switching the $i's$ and $j's$ in the derivative (i.e. $\partial u_i/\partial x_j \to \partial u_j/\partial x_i$), and the full strain tensor can be computed by summing $\partial u_i/\partial x_j$ and $\partial u_j/\partial x_i$. Computing the analytic expressions for the strain tensor produced by moment tensor sources results in expressions for P-waves and S-waves each consisting of three terms and a near-field expression. For the P-wave we have,

$$\epsilon_{ij}^{PF} = \frac{-1}{4\pi\rho\alpha^4}\frac{m\gamma_i\gamma_j}{r}\ddot{s}(t - r/\alpha) \tag{8a}$$

$$\epsilon_{ij}^{PI_1} = \frac{1}{4\pi\rho\alpha^3}\frac{m(\delta_{ij} - 10\gamma_i\gamma_j) + t\gamma_i\gamma_j + 4\Gamma_{ij}}{r^2}\dot{s}(t - r/\alpha) \tag{8b}$$

$$\epsilon_{ij}^{PI_2} = \frac{1}{4\pi\rho\alpha^2}\frac{m(6\delta_{ij} - 45\gamma_i\gamma_j) - t(\delta_{ij} - 6\gamma_i\gamma_j) + 24\Gamma_{ij} - 2M_{ij}}{r^3}s(t - r/\alpha) \tag{8c}$$

where equation (8a) is the far-field (r^{-1} dependence) P-wave term, and equations (8b) and (8b) are intermediate P-wavefield terms with r^{-2} and r^{-3} dependence respectively. Similarly, the expressions for the S-wave far-field and intermediate-field terms are,

$$\epsilon_{ij}^{SF} = \frac{1}{4\pi\rho\beta^4}\frac{m\gamma_i\gamma_j - \Gamma_{ij}}{r}\ddot{s}(t - r/\beta) \tag{9a}$$

$$\epsilon_{ij}^{SI_1} = \frac{-1}{4\pi\rho\beta^3}\frac{m(\delta_{ij} - 10\gamma_i\gamma_j) + t\gamma_i\gamma_j + 7\Gamma_{ij} - M_{ij}}{r^2}\dot{s}(t - r/\beta) \tag{9b}$$

$$\epsilon_{ij}^{SI_2} = \frac{-1}{4\pi\rho\beta^2}\frac{m(6\delta_{ij} - 45\gamma_i\gamma_j) - t(\delta_{ij} - 6\gamma_i\gamma_j) + 27\Gamma_{ij} - 3M_{ij}}{r^3}s(t - r/\beta) \tag{9c}$$

and the near-field term is,

$$\epsilon_{ij}^{NF} = \frac{1}{4\pi\rho}\frac{m(15\delta_{ij} - 105\gamma_i\gamma_j) - 3t(\delta_{ij} - 5\gamma_i\gamma_j) + 60\Gamma_{ij} - 6M_{ij}}{r^5}\int_{r/\alpha}^{r/\beta} \tau s(t-\tau)d\tau. \tag{10}$$

All of the terms above consist of a constant scalar multiplied by a fraction whose numerator is a term of varying complexity in the moment tensor M_{ij} and directional cosines γ_i, and whose denominator describes the wavefields decay with distance r. Together the constant scalar and the fraction it pre-multiplies describe the amplitude, its decay with distance, and the angle dependent radiation of seismic energy away from the source. This is then multiplied by a source time function, producing the strain tensor at a given distance r and point $\vec{x}$ in the subsurface.

P-wave terms

If the terms in equations (8a)-(8c) are those describing pure P-wave motion in a homogeneous medium, then they should produce no rotational motion (i.e. $\nabla \times \mathbf{u} = \mathbf{0}$ (e.g. Krebes, 2019)). Because our terms describe the strain tensor and not displacements, it is beneficial to rewrite this cross product in terms of the strain as,

$$\nabla \times \mathbf{u} = \begin{bmatrix} \partial u_3/\partial x_2 - \partial u_2/\partial x_3 \\ \partial u_1/\partial x_3 - \partial u_3/\partial x_1 \\ \partial u_2/\partial x_1 - \partial u_1/\partial x_2 \end{bmatrix} = 2\begin{bmatrix} \epsilon_{32} - \partial u_2/\partial x_3 \\ \epsilon_{13} - \partial u_3/\partial x_1 \\ \epsilon_{21} - \partial u_1/\partial x_2 \end{bmatrix}. \tag{11}$$

It may seem that in rewriting the curl in terms of strains, we have increased the complexity required to evaluate it. However, in deriving the expressions for the analytic strain for a P-wave, we have already computed the strain components and derivatives required to evaluate equation (11). If all of the terms that make up the derivatives $\partial u_i/\partial x_j$ are symmetric then,

$$\epsilon_{ij} = \frac{1}{2}\left(\frac{\partial u_i}{\partial x_j} + \frac{\partial u_j}{\partial x_j}\right) = \frac{\partial u_j}{\partial x_i} \tag{12}$$

and the curl, $\nabla \times \mathbf{u}$ will be $\vec{\mathbf{0}}$. The derivative contributing to the far-field P-wave term can be shown to be,

$$\frac{\partial u_i}{\partial x_j} \propto m\gamma_i\gamma_j = m\gamma_j\gamma_i \propto \frac{\partial u_j}{\partial x_i} \tag{13}$$

which satisfies the condition of a symmetric derivative, leading to $\nabla \times \mathbf{u} = \vec{\mathbf{0}}$ as expected for P-waves. It can be shown in a similar way that the other two P-wave terms also have symmetric derivatives, and therefore produce no rotational motion as expected.

S-wave terms

In contrast to P-waves, S-waves produce purely rotational motion, and no dilational motion (i.e. $\nabla \cdot \mathbf{u} = 0$). This is equivalent to saying that the trace of the strain tensor is zero, i.e. $\mathrm{tr}(\epsilon) = \epsilon_{11} + \epsilon_{22} + \epsilon_{33} = 0$. Evaluating the trace of the far-field S-wave term, we have,

$$\mathrm{tr}(\epsilon) \propto m(\gamma_1^2 + \gamma_2^2 + \gamma_3^2) - (\Gamma_{11} + \Gamma_{22} + \Gamma_{33}) = m - m = 0. \tag{14}$$

Where we made use of the fact that the vector γ_i is a unit vector with magnitude $\gamma_1^2 + \gamma_2^2 + \gamma_3^2 = 1$. Additionally, $\Gamma_{11} + \Gamma_{22} + \Gamma_{33} = m$ which can be shown in the following way:

$$\Gamma_{11} = \gamma_1 M_{1k} \gamma_k = \gamma_1 (M_{11}\gamma_1 + M_{12}\gamma_2 + M_{13}\gamma_3) \tag{15a}$$

$$\Gamma_{22} = \gamma_2 M_{2k} \gamma_k = \gamma_2 (M_{21}\gamma_1 + M_{22}\gamma_2 + M_{23}\gamma_3) \tag{15b}$$

$$\Gamma_{33} = \gamma_2 M_{2k} \gamma_k = \gamma_3 (M_{31}\gamma_1 + M_{32}\gamma_2 + M_{33}\gamma_3) \tag{15c}$$

$$\therefore \Gamma_{11} + \Gamma_{22} + \Gamma_{33} = \gamma_p M_{pq} \gamma_q = m \tag{15d}$$

Carrying out the same analysis on the other two S-wave terms shows that the trace of their general strain tensor, and therefore dilatation are also zero. Thus all three terms that travel with velocity β, equations (9a)-(9c), produce purely rotational motion which is consistent with purely S-wave propagation in a homogeneous medium.

Analytic modeling

The above analysis precludes modeling in complex media, especially of the type that develops as hydraulic fracturing treatments progress. However, these equations contain important insights into the character of the seismic waves produced by engineered fractures and earthquakes. Typically, the traveltime differences in the P-wave and S-wave first arrivals are used to localize fractures and earthquakes. Analytic modeling provides an efficient means of modeling these direct arrivals. Perhaps the most important feature of the analytic modeling expressions is the far-field P-wave and S-wave radiation patterns which can be used to predict moment tensor source types, and gain an understanding of the fault mechanism (Eaid et al., 2020).

Radiation patterns

The analytic expressions for the strain radiated by moment tensor sources in equations (8a)-(10) have the form,

$$c\frac{R_p}{r^n}\frac{\partial^k s(t - r/v)}{\partial t^k} \tag{16}$$

where c is a constant that is dependent on the medium density and P-wave (α) or S-wave velocity (β), r^n is the distance between source and receiver to the n^{th} power, $\partial^k s(t-r/v)/\partial t^k$ is the k^{th} partial derivative of the source function with respect to time, and R_p, which is a function of the moment tensor M and the directional cosines between the source and receiver, is known as the radiation pattern. Consider a unit sphere of uniformly distributed strain sensors, and temporarily assume that these strain sensors have independent access to each component of the strain tensor. If we neglect the effects of geometric spreading and the source time function, the response of these sensors describes the seismic energy generated by a given moment tensor M as a function of the angle $\gamma = \mathbf{x}/r$ between the source and receiver.

For a given source-receiver pair, the angle γ is consistent for varying source mechanisms. Thus, the source mechanism controls the angular radiation of seismic energy. Figure 1 plots the ϵ_{xx} component of these radiation patterns for the P-wave and S-wave motions generated by an explosive source in Figures 1a and 1e, for the P-wave and S-wave motions generated by a tensile crack source in Figures 1b and 1f, for the P-wave and S-wave motions generated by a compensated linear vector dipole (CLVD) source in Figures 1c and 1g, and for the P-wave and S-wave motions generated by a double couple source in Figures 1d and 1h. The moment tensors for each of these source types expressed as the six independent components $\mathbf{M}_{\text{T}} = \{M_{xx}, M_{xy}, M_{xz}, M_{yy}, M_{yz}, M_{zz}\}$ are :

$$\begin{aligned} \mathbf{M}_{\text{EXP}} &= \{1,0,0,1,0,1\} \\ \mathbf{M}_{\text{TC}} &= \{2,0,0,3,0,2\} \\ \mathbf{M}_{\text{CLVD}} &= \{-1,0,0,2,0,-1\} \\ \mathbf{M}_{\text{DC}} &= \{0,1,0,0,0,0\} \end{aligned} \tag{17}$$

Consider a straight fiber in a horizontal well that is oriented in the x-direction so that only the ϵ_{xx} component of the strain tensor is sensed. Figure 2a plots the trajectroy of a well having this geometry; Figure 2b-2e plots the seismic data recored by a fiber in this well for the four source types generatring the radiation patterns in Figure 1. Provided a sufficient solid angle of the unit sphere surrounding the source is sampled, then the data contain sufficient angular variation in the amplitude and polarity such that predictions can be made about the source mechanism (Eyre and van der Baan, 2015). Eaid et al. (2020), in this issue, use equation (8a) and (9a) to model synthetic data which is used as input to a machine learning study focused on moment tensor estimation. The extension of their synthetically trained neural network to field data shows the power of analytically modeled data, despite its preclusion to modeling in complex geology.

Near-field and far-field dominance

Each of the terms in equations (8a)-(10) decays as function of the distance from the source r. Equations (8a) and (9a) are the far-field P-wave and S-wave terms, so named because they travel at the P-wave and S-wave velocity respectively, and decay with r^{-1}, allowing them to dominate the other terms far from the source. Because of this, the far-field P-waves and S-waves are typically the body wave component measure during fracture

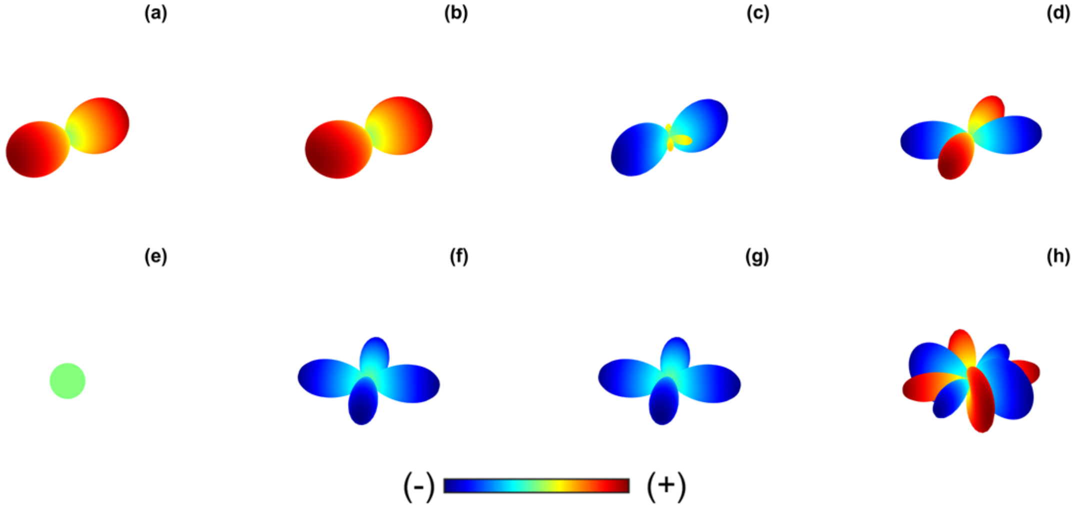

FIG. 1. The ϵ_{xx} component of the analytic strain radiation patterns for four source types. P-wave radiation patterns for (a) $\mathbf{M}_{\text{EXP}}$, (b) $\mathbf{M}_{\text{TC}}$, (c) $\mathbf{M}_{\text{CLVD}}$, (d) $\mathbf{M}_{\text{DC}}$. S-wave radiation patterns for (e) $\mathbf{M}_{\text{EXP}}$, (f) $\mathbf{M}_{\text{TC}}$, (g) $\mathbf{M}_{\text{CLVD}}$, (h) $\mathbf{M}_{\text{DC}}$.

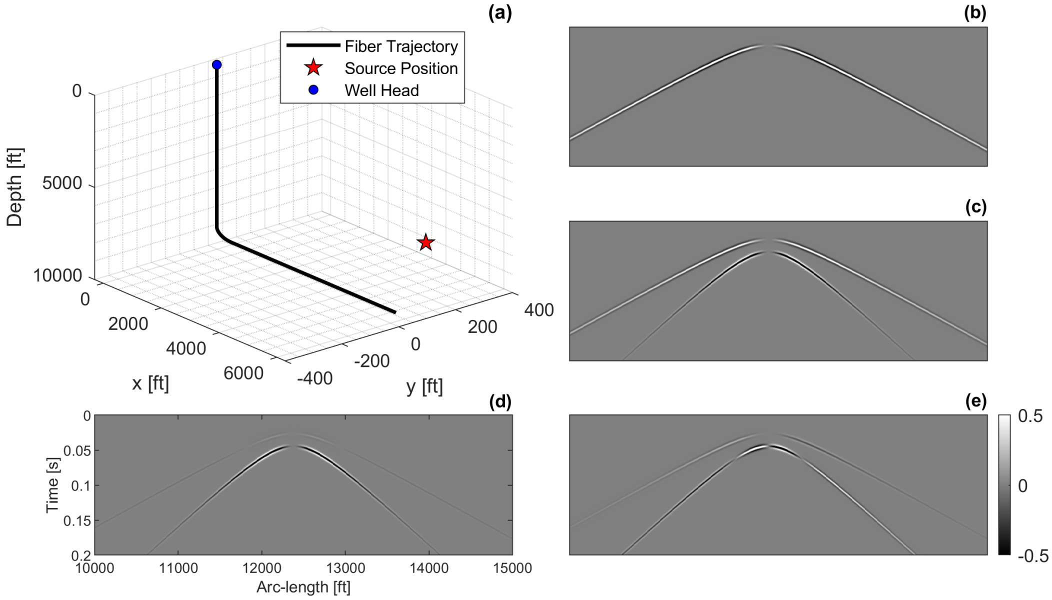

FIG. 2. (a) Schematic representation of the fiber trajectory shown by the black line, and the source location indicated by the red star. Data recoded by the fiber for (b) $\mathbf{M}_{\text{EXP}}$, (c) $\mathbf{M}_{\text{TC}}$, (d) $\mathbf{M}_{\text{CLVD}}$, and (e) $\mathbf{M}_{\text{DC}}$.

propagation or fault initiation. However, DAS places sensors much closer to the source locations, especially during hydraulic fracturing, potentially leading to measurement of the near-field term in equation (10), which is dominate close to the source. The region around the source in which the near-field term dominates is important to study.

Consider the source-time function,

$$s(t) = \frac{T^2}{T^2 + t^2} \tag{18}$$

where T the half-width at half the maximum value of the pulse, and t is the time after source excitation. This source time function and its first two time derivatives are plotted in Figure 3a-3c.

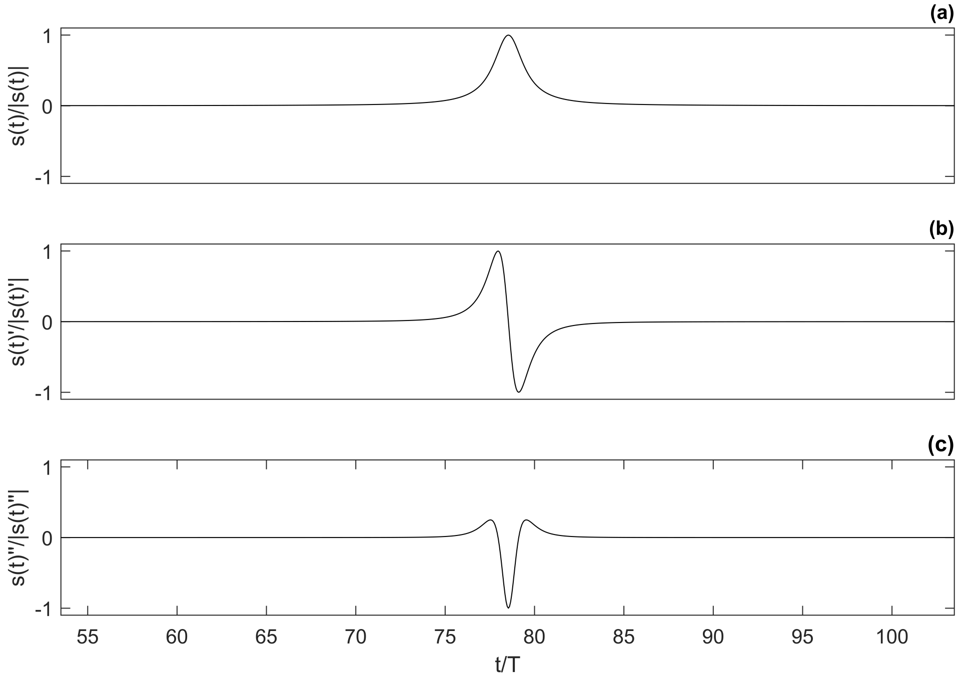

FIG. 3. (a) Displacement source time function from equation (18), (b) normalized first time derivative $s'(t)$ of the source time function normalized, and (c) normalized second time derivative $s''(t)$ of the source time function.

Using this source time function and its time derivatives as input to equations (8a)-(10), and plotting traces at various distances r from the source allows us to investigate the contribution of near-field and far-field terms. Eaton et al. (2010) show that the near field term for the analytic displacement dominates within approximately one-wavelength of the source. Using medium properties of V_p = 4000 m/s, V_s = 2000 m/s, and $T = 1.6E-2$ leading to a dominant frequency of 100 Hz for the velocity component, the near-field displacement should dominate within the 40 meter range.

Figures 4a, 4c, and 4e plot the full-field displacement for distances of 40 meters, 200 meters, and 500 meters from the source, while Figures 4b, 4d, and 4f plot the near-field components in red, and the far-field components in blue. At 40 meters from the source, approximately one-wavelength, the near-field component is dominate and changes the shape of the pulse while masking the occurrence of the P-wave. At 100 meters, the P-wave and S-wave are identifiable but the near-field is still relatively large, manifesting in low frequency energy between the P-wave and S-wave arrivals. At 500 meters, the near-field has become relatively small. In contrast Figures 5a, 5c, and 5e plot the full-field strain for distances of

40 meters, 200 meters, and 500 meters from the source, while Figures 5b, 5d, and 5f plot the near-field components in red, and the far-field components in blue. It is evident that the near-field strain does not dominate at any of the three distances.

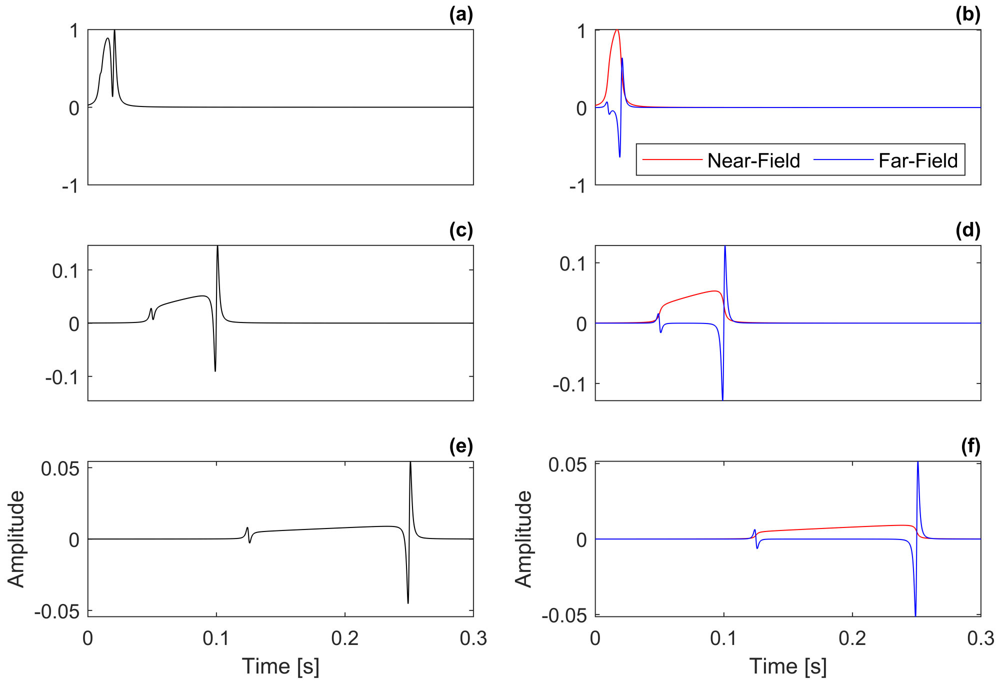

FIG. 4. (a) Full-field displacement for $r = 40$ meters, (b) near-field (red) and far-field (blue) displacement for $r = 40$ meters, (c) full-field displacement for $r = 100$ meters, (d) near-field (red) and far-field (blue) displacement for $r = 100$ meters, (e) full-field displacement for $r = 500$ meters, (f) near-field (red) and far-field (blue) displacement for $r = 500$ meters.

The far-field strain is a function of the particle acceleration $\ddot{(s)}(t)$, which has a higher frequency ($f_{\text{MAX}} = 200$ Hz) than the velocity component that the far-field displacement is a function of. The near-field strain also decays faster, being a function of r^{-4}, than the displacement . Figure 6a plots the full-field strain and Figure 6 the near-field strain for a distance of $r = 18$ meters, which is approximately one-wavelength for the P-wave component of the particle acceleration. At this distance from the source, the near-field becomes more dominant, masking the P-wave arrival which is beginning to separate from the S-wave arrivals and changing the overall shape of the pulse. This analysis suggests that the near-field strain terms are also only dominant within approximately one wavelength from the source, but that the wavelength is much smaller due to the higher frequency nature of far field strain.

VELOCITY-STRESS FINITE DIFFERENCE METHOD

The incorporation of complex geology in modeling DAS signals from microseismic moment tensor sources requires treatment with finite-difference methods. Eaid et al. (2017) coupled geometric models of the fiber to a 3D finite-difference elastic wave propagator based on the velocity-stress method (Virieux, 1986). Eaid et al. (2017) provides a detailed analysis of how to model DAS signals with this method, for brevity only the key components are summarized here. The elastodynamic equation of motion is,

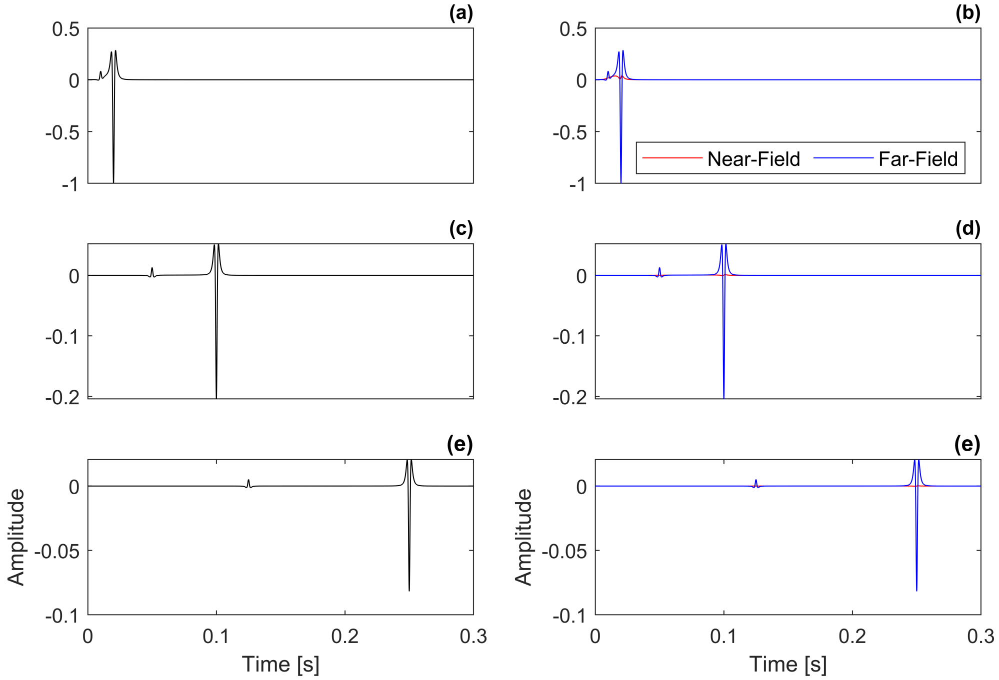

FIG. 5. (a) Full-field strain for $r = 40$ meters, (b) near-field (red) and far-field (blue) strain for $r = 40$ meters, (c) full-field strain for $r = 200$ meters, (d) near-field (red) and far-field (blue) strain for $r = 200$ meters, (e) full-field strain for $r = 500$ meters, (f) near-field (red) and far-field (blue) strain for $r = 500$ meters.

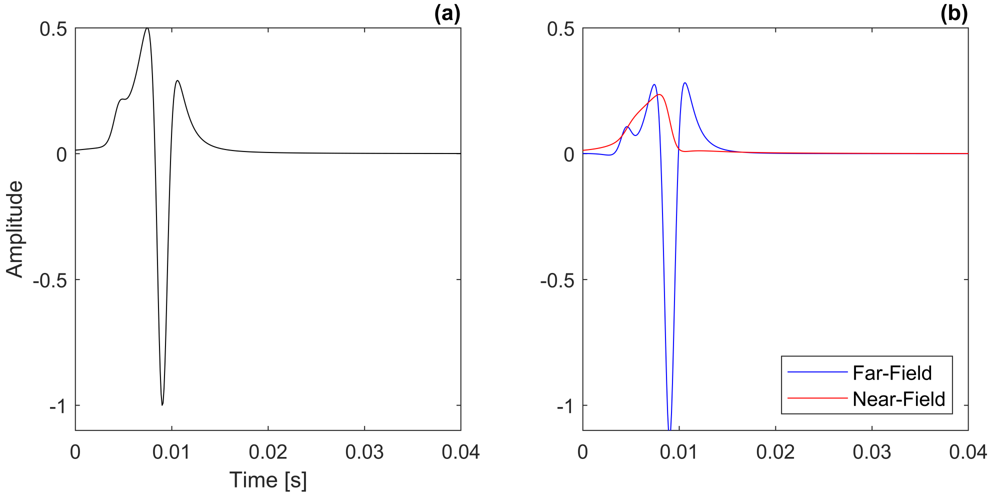

FIG. 6. (a) Full-field strain for $r = 18$ meters, (b) far-field (blue) and near-field (red) strain for $r = 18$ meters.

$$\nabla \cdot \sigma + \mathbf{f} = \rho \frac{\partial \mathbf{v}}{\partial t} \tag{19}$$

where $\mathbf{v}$ is the particle velocity, $\mathbf{f}$ is the source function, and σ is the stress tensor defined through Hooke's Law as,

$$\sigma = \mathbf{C}\epsilon \tag{20}$$

with the strain tensor ϵ defined by equation (1), and $\mathbf{C}$ is the stiffness tensor. Subbing the stress-strain relation (Hooke's Law) in equation (19) defines the equation of motion in terms of strain,

$$\nabla \cdot (\mathbf{C}\epsilon) + \mathbf{f} = \rho \frac{\partial \mathbf{v}}{\partial t}. \tag{21}$$

In practice, solving equation (21) alternates between computing the strain and particle velocity on staggered grids. At each time step, the strains are projected onto the fiber tangents using equation (4).

Moment tensor sources in the velocity-stress method

This paper is interested in modeling signals of the type recorded during microseismic monitoring or for future applications in seismological studies. To accomplish this, we require a method for inclusion of moment tensor type source functions for $\mathbf{f}$ in equation (21). Each component of the moment tensor is defined by a force couple f_i acting in the i^{th} direction, separated by a small distance δx_j in the j^{th} direction,

$$M_{ij}(t) = f_i(t)\delta x_j. \tag{22}$$

Equation (22) suggests that finite-difference methods can incorporate the moment tensor by the defining each component of the source time function as,

$$f_i(t) = \sum_j \frac{M(t)_{ij}}{\delta x_j} \hat{x}_j. \tag{23}$$

In this paper, following Frankel (1993) and Graves (1996), the source terms in equation (23) are applied to the velocity components.

To compare the finite-difference simulation to the analytically simulated waves, we propagate a wavefield through a homogenous medium with $V_p = 4000$ m/s, and $V_s = 2000$ m/s, and compare a snapshot of this wavefield to analytically modeled radiation patterns. These simulations are carried out using the double couple moment tensor $\mathbf{M}_{\text{DC}} = \{0, 1, 0, 0, 0, 0\}$ Figure 7a-7f plot a snapshot of the wavefiled for ϵ_{xx}, ϵ_{yy}, ϵ_{zz}, ϵ_{xy}, ϵ_{xz}, and ϵ_{yz}. Figures 8a-8f plot the P-wave component of the analytic radiation patterns for ϵ_{xx}, ϵ_{yy}, ϵ_{zz}, ϵ_{xy}, ϵ_{xz}, and ϵ_{yz}. Figures 9a-9f plot the plot the same for the S-wave component. Comparison of these figures show similar radiation of the P-wave and S-wave components for both the analytic and numerical experiments lending further evidence that equations (8a) and (9a) are the far-field P-wave and S-wave modes radiated by moment tensor sources.

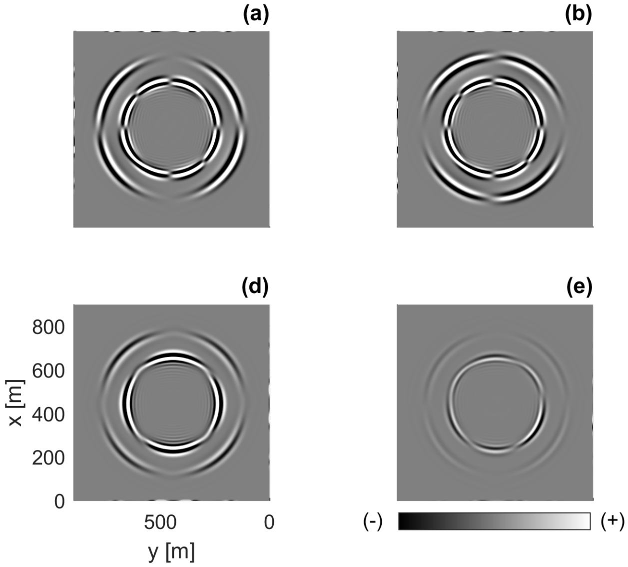

FIG. 7. Finite-difference strain wavefields radiated by $\mathbf{M}_{\text{DC}}$. (a) ϵ_{xx}, (b) ϵ_{yy}, (c) ϵ_{zz}, (d) ϵ_{xy}, (e) ϵ_{xz}, (f) ϵ_{yz}

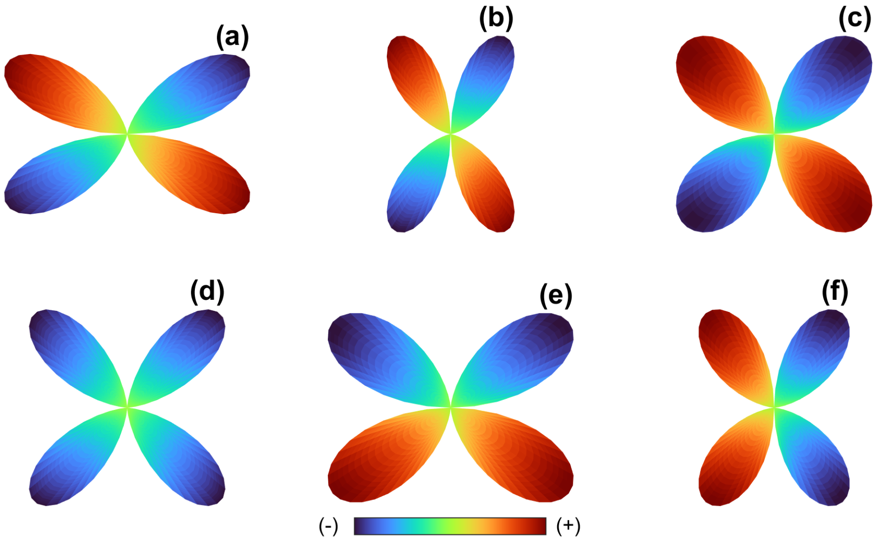

FIG. 8. P-wave component of the analytic strain wavefields radiated by $\mathbf{M}_{\text{DC}}$. (a) ϵ_{xx}, (b) ϵ_{yy}, (c) ϵ_{zz}, (d) ϵ_{xy}, (e) ϵ_{xz}, (f) ϵ_{yz}

We also consider another example of in which a compensated linear vector dipole (CLVD) source with components $\mathbf{M}_{\text{CLVD}} = \{1, 0, 0, -2, 0, 1\}$. Figures 10-12 plot the same results as Figures 7-9 for the CLVD source. Again the numerical and analytically results are strongly correlated.

COMPARISON TO FIELD DATA

The analytic and finite-difference modeling methods presented above produce similar strain field radiations lending confidence that the two methods are comparable. To ensure that the two methods can accurately model field data of the type that may be acquired during

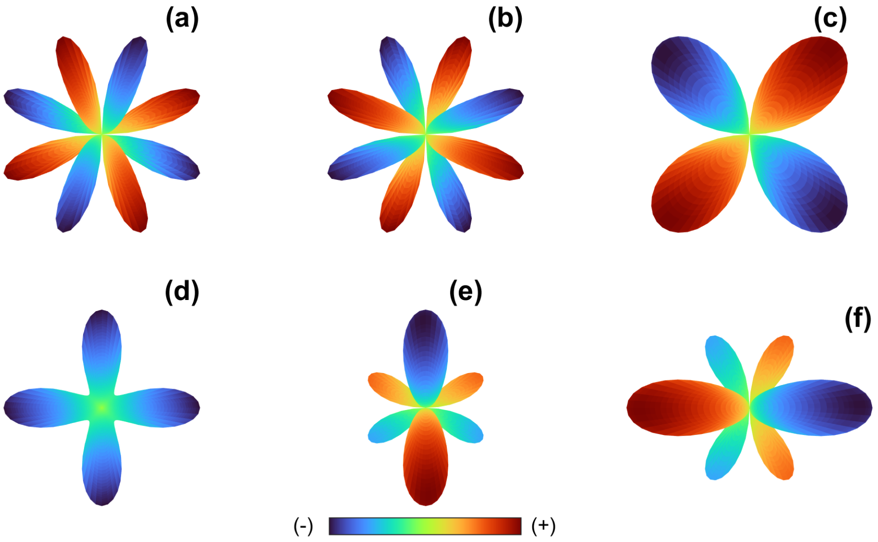

FIG. 9. S-wave component of the analytic strain wavefields radiated by $\mathbf{M}_{\mathrm{DC}}$. (a) ϵ_{xx}, (b) ϵ_{yy}, (c) ϵ_{zz}, (d) ϵ_{xy}, (e) ϵ_{xz}, (f) ϵ_{yz}

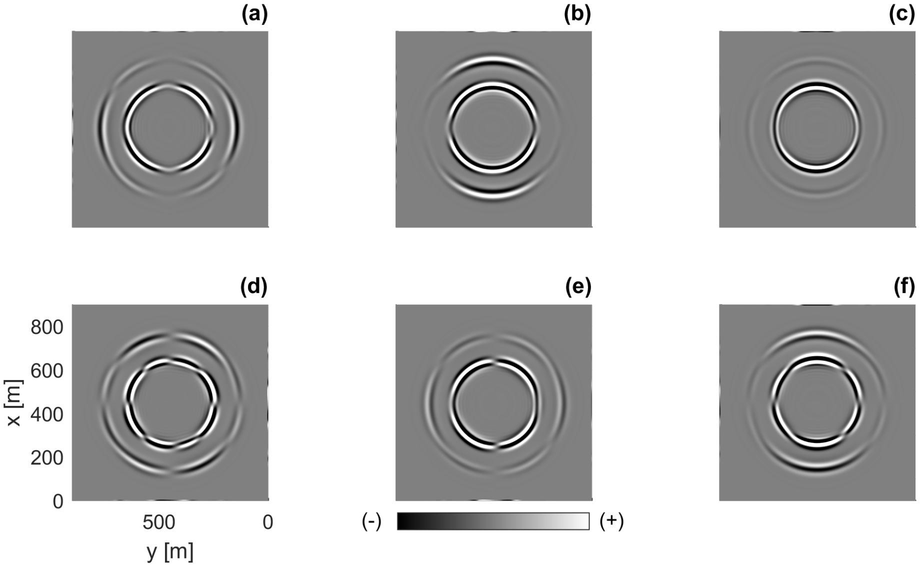

FIG. 10. Finite-difference strain wavefields radiated by $\mathbf{M}_{\mathrm{CLVD}}$. (a) ϵ_{xx}, (b) ϵ_{yy}, (c) ϵ_{zz}, (d) ϵ_{xy}, (e) ϵ_{xz}, (f) ϵ_{yz}

hydraulic fracturing we use each method to simulate data and compare the data to a field event from a DAS-microseismic dataset plotted in Figure 14(a). Consider a horizontal well with length of 5700 feet at a depth of 9300 feet containing a length of straight DAS fiber embedded in a homogeneous medium with $V_p = 15600$ feet/s, and $V_s = 9530$ feet/s. Figure 14(b) plots the analytically modeled DAS data from this model using the prescribed fiber geometry. We also consider a slightly more complex medium plotted in Figure 13, where the velocities in the layer containing the fiber are the same as those in the homogeneous medium. Figure 14(c) plots the data from the layered model computed using the velocity-stress finite-difference method. Both datasets were modeled with the moment tensor

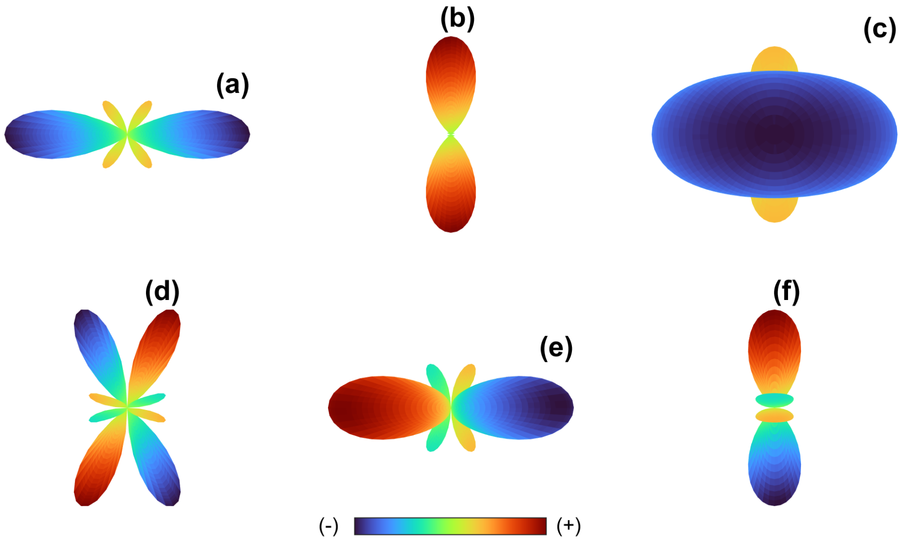

FIG. 11. P-wave component of the analytic strain wavefields radiated by $\mathbf{M}_{\text{CLVD}}$. (a) ϵ_{xx}, (b) ϵ_{yy}, (c) ϵ_{zz}, (d) ϵ_{xy}, (e) ϵ_{xz}, (f) ϵ_{yz}

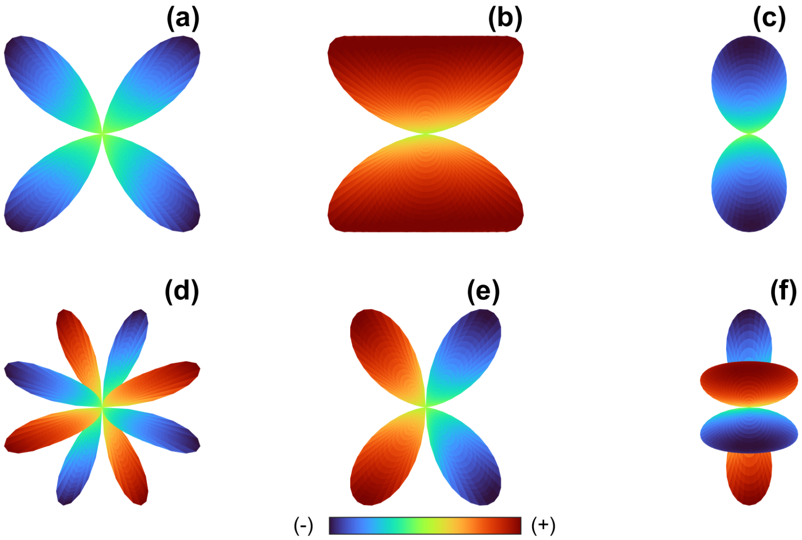

FIG. 12. S-wave component of the analytic strain wavefields radiated by $\mathbf{M}_{\text{CLVD}}$. (a) ϵ_{xx}, (b) ϵ_{yy}, (c) ϵ_{zz}, (d) ϵ_{xy}, (e) ϵ_{xz}, (f) ϵ_{yz}

$$\mathbf{M} = \begin{bmatrix} 0.69 & 1.00 & -0.69 \\ 1.00 & 0.35 & -0.22 \\ -0.69 & -0.22 & 0.69 \end{bmatrix} \tag{24}$$

which estimated from the field data by Eaid et al. (2020) using their deep learning method. Both modeled datasets capture the important features of the field data. For example, both have the distinct polarity pattern of the field data S-wave, and both show attenuation of the P-wave to the toe side of the well (right side of Figure 14). Additionally, the numerically modeled data captures some of the complexity in the field data such as head waves from the

S-wave modes refracting from the upper and lower interfaces of the layer containing the fiber, as well as reflections which are buried in noise in the field data. The strong correlation between the field data and modeled datasets is encouraging and suggests the use of these modeling techniques is a viable strategy for modeling DAS-microseismic data.

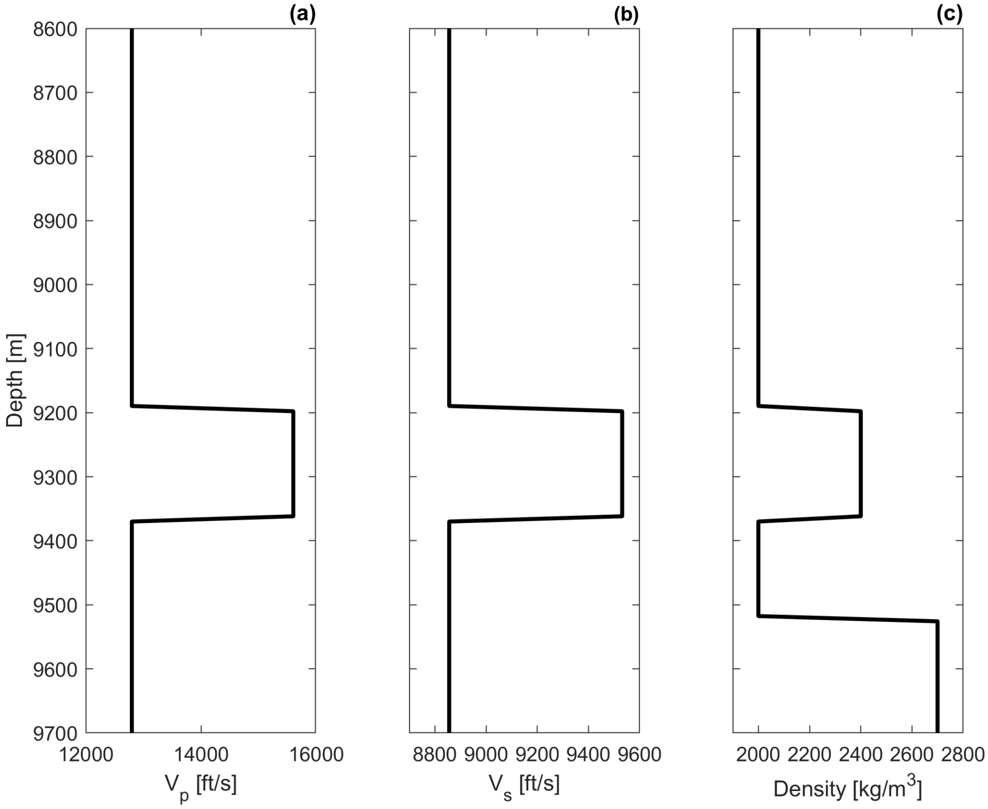

FIG. 13. (a) V_p model for finite-difference simulation, (b) V_s model for finite-difference simulation, (c) density model for finite-difference simulation.

CONCLUSIONS

With the rapid advancement of DAS for reservoir monitoring and earthquake seismology, methods for modeling DAS data from moment tensor type sources are required to enhance our understanding of these complex datasets. In this paper we present two methods for modeling strain fields in media of differing complexity and couple each to geometric models of DAS fibers to simulate DAS data. The first is an analytic method for modeling the strain field generated by a general moment tensor source, which is limited to modeling in homogeneous media, but is very efficient for modeling large datasets of direct arrival information. The second is an extension of the velocity-stress finite-difference method to modeling strain fields with the incorporation of moment tensor source distributions. Both methods are compared to each other, and produce similar direct arrival information. Each method has distinct advantages dependent on the type of data modeling that is desired. We then use each method to simulate data using the geometry of a field deployed DAS fiber and a source mechanism predicted by Eaid et al. (2020). Each method simulates data which correlates well to the field data suggesting the modeling algorithms presented here can be used

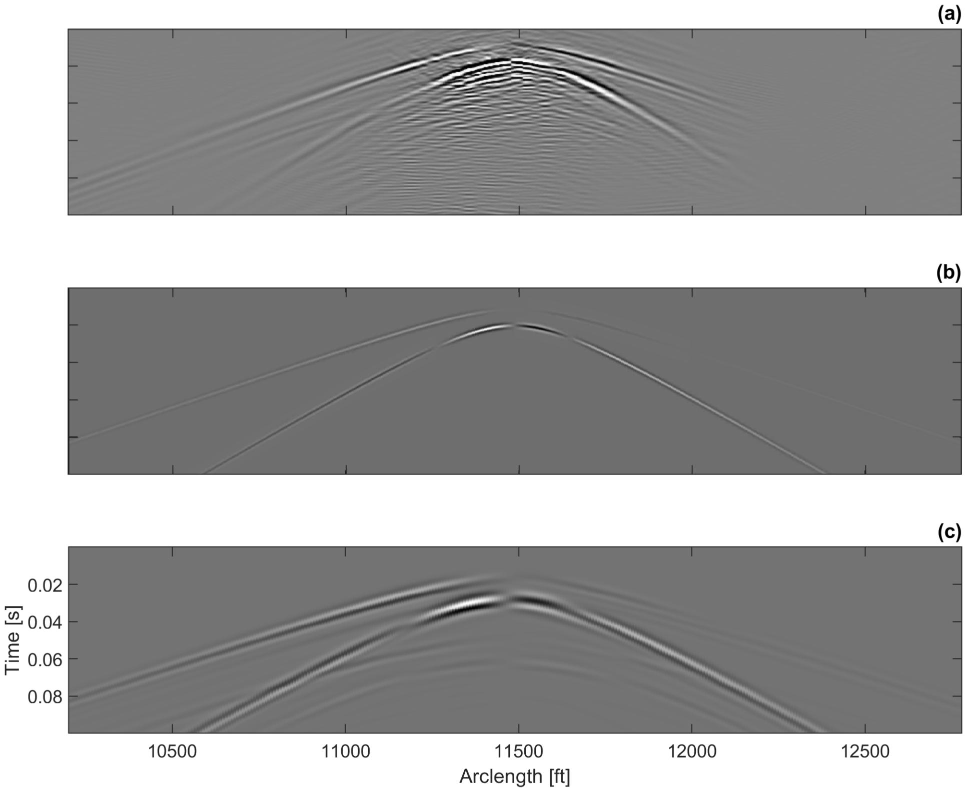

FIG. 14. (a) Field data event from DAS-microseismic dataset, (b) analytically modeled DAS data, (c) DAS data modeled through the velocity-stress finite-difference method. Note that the numerical finite-difference data was modeled with a lower frequency (110 Hz) wavelet due to computational restrictions.

to simulate field data. It is expected that these algorithms will be used to simulate datasets for further studies involving imaging and inversion. Another communication in this issue (Eaid et al., 2020) uses the analytic modeling method presented here to efficiently model a large datasets for a DAS-microseismic study focused on using deep learning techniques for source mechanism estimation.

ACKNOWLEDGMENTS

The authors would like to thank the sponsors of the CREWES project as well NSERC under the grants CRDPJ 461179-13 and CRDPJ 543578-19 for making this work possible through their financial support. Matt Eaid is partially supported through scholarships from the SEG foundation.

REFERENCES

Aki, K., and Richards, P., 2002, Quantitative Seismology: University Science Books, 2 edn.

Eaid, M., Hu, C., Zhang, L., Keating, S., and Innanen, K., 2020, Estimation of das microseismic source mechanisms using unsupervised deep learning: CREWES Research Reports, **32**, No. 8.

Eaid, M., Li, J., and Innanen, K., 2017, A coupled DAS shaped-fiber and 3D elastic finite difference wave model: CREWES Research Reports, **29**, No. 12, 1–19.

Eaton, D., Forouhideh, F., and van der Baan, M., 2010, Spectral and near-field characteristics of induced microseismicity: CSPG GeoCanada 2010 Conference Abstract.

Eyre, T. S., and van der Baan, M., 2015, Overview of moment-tensor inversion of microseismic events: The Leading Edge, **34**, No. 8, 882–888.

Frankel, A., 1993, Three-dimensional simulations of ground motions in the San Bernardino Valley, California, for hypothetical earthquakes on the San Andreas fault: Bulletin of the Seismological Society of America, **83**, No. 4, 1020–1041.

Graves, R. W., 1996, Simulating seismic wave propagation in 3D elastic media using staggered-grid finite differences: Bulletin of the Seismological Society of America, **86**, No. 4, 1091–1106.

Krebes, S., 2019, Seismic Wave Theory: Cambridge University Press, 1 edn.

Lindsey, N. J., Martin, E. R., Dreger, D. S., Freifeld, B., Cole, S., James, S. R., Biondi, B. L., and Ajo-Franklin, J. B., 2017, Fiber-optic network observations of earthquake wavefields: Geophysical Research Letters, **44**, No. 23, 11,792–11,799.

Virieux, J., 1986, P-sv wave propagation in heterogeneous media: VelocityâĂŘstress finiteâĂŘdifference method: Geophysics, **51**, No. 4, 889–901.

Webster, P., Wall, J., Perkins, C., and Molenaar, M., 2013, Micro-seismic detection using distributed acoustic sensing: SEG Technical Program Expanded Abstracts 2013, 2459–2463.

Yu, C., Zhan, Z., Lindsey, N. J., Ajo-Franklin, J. B., and Robertson, M., 2019, The potential of das in teleseismic studies: Insights from the goldstone experiment: Geophysical Research Letters, **46**, No. 3, 1320–1328.